0191-8141(95)00024-0

Estimation of non-coaxiality from crinoid-type pressure fringes: comparison between natural and simulated examples

KAZUHIKO ISHII

Division of Natural Science, Osaka Kyoiku University, Asahigaoka, Kashiwara, Osaka 582, Japan

Abstract—The development of rigid crinoid-type pressure fringes is simulated for variable shape and orientation of the rigid original grains, matrix flow pattern and total strain, using Etchecopar and Malavieille's model, which is based on a principle of geometrical minimization of the gap between a rigid grain and its ductile matrix. A method of determining the non-coaxiality of the matrix flow is constructed assuming two-dimensional flow with constant area and time-independent flow parameters. In this method, the systematic variation in the geometry of the pressure fringes as a function of the shape and orientation of the rigid original grains, is used as a criterion. The application to the natural examples shows consistent variation in the geometry of pressure fringes with the simulation. This indicates the validity of the method as long as the assumptions hold.

INTRODUCTION

The kinematic description of rock flow is indispensable to an understanding of the dynamics of the crust and mantle of the Earth. Although many attempts have been made in the past to reconstruct deformation paths and to determine flow parameters such as shear sense and degree of non-coaxiality in rocks (e.g. Elliott 1972, Durney & Ramsay 1973, Cox & Etheridge 1983, Lister & Williams 1983, Simpson & Schmid 1983, Lister & Snoke 1984, Hanmer 1986, Passchier 1986, 1988, 1990, Passchier & Simpson 1986, Cobbold *et al.* 1987, Dennis & Secor 1987, Goldstein 1988, Bjornerud 1989, Williams & Price 1990, Passchier & Sokoutis 1993, Simpson & De Paor 1993), complexities in kinematic analysis become increasingly recognized (e.g. Ishii 1992).

Pressure fringes are fibrous minerals (generally quartz, calcite, chlorite and muscovite) developed around grains more rigid than their matrix. They are widely developed in deformed rocks up to greenschist facies. The difference in rheological properties between the grain and the matrix leads to discordance in the displacement field at the grain boundary and the gaps so created are filled by fibrous minerals.

Pressure fringes have been classified into three types according to the growth direction of the fibres: pyrite type (antitaxial), crinoid type (syntaxial) and composite type (Durney & Ramsay 1973, Ramsay & Huber 1983), and they have been further divided into rigid and deformable types depending on the rheological behavior of the fibrous material (Ramsay & Huber 1983). There may exist continuous variation between these two end-members. In addition, Durney & Ramsay (1973) and Ramsay & Huber (1983) have distinguished between displacement-controlled and face-controlled fibre growth. In the latter, the length direction of the fibres is not parallel to the displacement direction, although inclusion trails (ghost fibres) indicate the displacement direction (see also Ramsay 1980, Cox & Etheridge 1983,

Cox 1987). This information about the displacement direction is essential to kinematic analysis.

Previous studies using pressure fringes as kinematic indicators of rock deformation can be divided into two groups. One aims at the sequential determination of strain increments (Elliott 1972, Durney & Ramsay 1973, Wickham 1973, Ramsay & Huber 1983, Beutner & Diegel 1985, Ellis 1986, Spencer 1991). The other aims at the determination of several parameters by comparison of the total geometry with simulated pressure fringes (Etchecopar & Malavieille 1987, Malavieille & Ritz 1989).

The first approach has the advantage of obtaining a strain path in a deterministic manner. The second approach requires a method of trial and error to match the simulated pressure fringe with the natural one. An advantage of this approach is the ability to incorporate the rotation of the rigid grain as a function of matrix flow and grain shape. This advantage is revealed in the excellent reproduction of the variable geometry of natural pressure fringes using a small number of parameters and actual grain shapes (Etchecopar & Malavieille 1987, Malavieille & Ritz 1989).

Etcheopar & Malavieille (1987) constructed a simulation model for pyrite-type pressure fringes. In this paper, rigid crinoid-type pressure fringes are simulated using the same model. Then, using systematic variations in the geometry of pressure fringes as a function of the shape and orientation of the rigid grain, a method to determine non-coaxiality is constructed and is applied to natural examples.

DESCRIPTION OF FLOW

Flow can be described by the velocity gradient tensor L as a function of time and position. L can be decomposed into a symmetrical rate of deformation tensor D and an antisymmetrical vorticity tensor W':

$$L_{ij} = D_{ij} + W'_{ij}, \qquad (1)$$

where

$$D_{ij} = \tfrac{1}{2}(L_{ij} + L_{ji}), \text{ and}$$

$$W'_{ij} = \tfrac{1}{2}(L_{ij} - L_{ji}).$$

The orientation of the eigenvectors of D correspond to the instantaneous stretching axes (ISA) of the flow and the eigenvalues of D correspond to the principal stretching rates. W' represents the rotational component of the flow (i.e. average angular velocity of all material lines) with respect to the reference frame. W' can be further decomposed into an internal vorticity W and a spin Ω (Means et al. 1980, Lister & Williams 1983),

$$L_{ij} = D_{ij} + W_{ij} + \Omega_{ij}. \qquad (2)$$

Ω describes the rotation rate of the ISA with respect to the reference frame and W describes the average rotation rate of material lines relative to the ISA (internal frame). Note that although Ω is different in different frames, W is independent of the reference frame in which the flow is described.

The non-coaxiality of the flow can be defined by the kinematical vorticity number, which was introduced by Truesdell (1953) and redefined for internal vorticity only by Means et al. (1980);

$$W_k = \frac{W}{\sqrt{2(s_1^2 + s_2^2 + s_3^2)}} = \frac{W}{S}, \qquad (3)$$

where W is the magnitude of the internal vorticity vector and s_i are the eigenvalues of D. S is a measure of stretching rate, then W_k is the ratio of the instantaneous magnitudes of the internal vorticity and stretching rate. Detailed explanations of these flow parameters and their geological implications are given in Means et al. (1980), Lister & Williams (1983), Passchier (1986) and Ishii (1992).

In this paper, the matrix flow is assumed to be two dimensional and maintaining constant area, with time-independent flow parameters, and is described in the reference frame which is parallel to the ISA (i.e. no spin component). In this case, without losing generality, the flow can be represented by

$$L = D + W = \begin{pmatrix} e & 0 \\ 0 & -e \end{pmatrix} + \begin{pmatrix} 0 & w \\ -w & 0 \end{pmatrix}, \qquad (4)$$

where $e \geqslant 0$ and $w \geqslant 0$ (Fig. 1), and non-coaxiality (3) is given by

$$W_k = \frac{w}{e}. \qquad (5)$$

In this paper, clockwise rotation is taken to be positive.

ROTATION OF A RIGID GRAIN IN A FLOWING MATRIX

A rigid elliptical grain embedded in a flowing viscous medium rotates. For a case of matrix flow given by
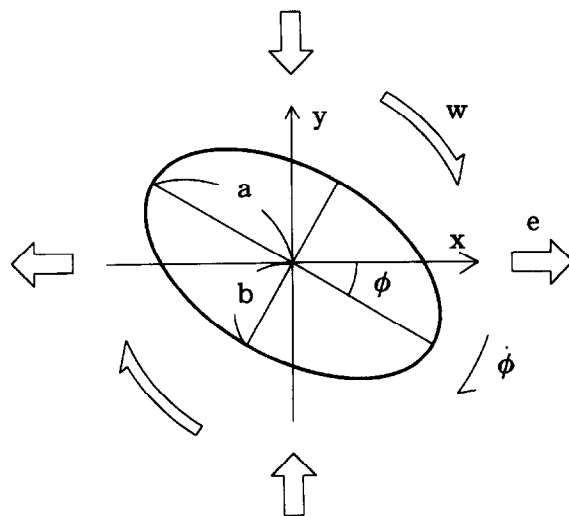

Fig. 1. Definition of parameters. The reference frame (xy-axes) is parallel to the ISA of the matrix flow. w and e are the components of the velocity gradient tensor for the matrix flow (equation 4). a and b are lengths of the long and short axes of a rigid elliptical grain, and $R = a/b$ defines the ellipticity of the grain. ϕ and $\dot{\phi}$ represent the orientation of the long axis and the rotation rate of the grain.

equation (4), the rotation rate of the grain is (Jeffery 1922, Ghosh & Ramberg 1976)

$$\dot{\phi} = \dot{\phi}_D + \dot{\phi}_W = \left[-e\frac{R^2 - 1}{R^2 + 1}\sin 2\phi \right] + [w], \qquad (6)$$

where R and ϕ are ellipticity and orientation of the elliptical grain, respectively (Fig. 1). $\dot{\phi}_D$ represents the rotation rate due to the D component of the velocity gradient tensor and is a function of e, R and ϕ. $\dot{\phi}_W$ represents the rotation rate due to the W component and is independent of R and ϕ.

For a circular grain ($R = 1$), the rotation rate of the grain is equal to w because $\dot{\phi}_D$ vanishes. Elliptical grains ($R > 1$) will rotate even if the flow is coaxial (i.e. $w = 0$). In such coaxial flow, the elliptical grain with orientations of $\phi < 0°$ and $\phi > 0°$ rotates clockwise and anti-clockwise, respectively. The absolute magnitude of the rotation rate is a maximum at $\phi = \pm 45°$ and vanishes at $\phi = 0°$ and $\pm 90°$. For given e and ϕ in coaxial flow, the absolute magnitude of the rotation rate of the grain increases with R.

In general flow, the rotation rate of an elliptical grain is the sum of $\dot{\phi}_D$ and $\dot{\phi}_W$, and thus, a function of R, ϕ and W_k. Therefore, the rotation rate is a maximum at $\phi = -45°$ and a minimum at $\phi = 45°$, including negative values. From equation (6), the condition for anticlockwise rotation ($\dot{\phi} < 0$) is given by

$$\frac{R^2 - 1}{R^2 + 1}\sin 2\phi > \frac{w}{e} = W_k. \qquad (7)$$

If $W_k \geqslant 1$, all grains rotate clockwise irrespective of the values of R and ϕ. Furthermore, the elliptical grain with

$$\frac{R^2 - 1}{R^2 + 1} > W_k \qquad (8)$$

rotates anticlockwise at an orientation of around $\phi = 45°$, because $\sin 2\phi$ has its maximum value of 1 at

$\phi = 45°$. The range of ϕ for which the grain rotates anticlockwise increases with increasing R and decreasing W_k. Detailed explanations and graphical presentations are given in Ghosh & Ramberg (1976).

Using model experiments, Ghosh & Ramberg (1976) showed that these equations also apply to non-elliptical rigid grains, such as rectangular grains, with a suitable approximation of the shape by ellipses.

METHOD OF SIMULATION

The development of rigid crinoid-type pressure fringes is simulated using the computer model of Etche-copar & Malavieille (1987). The matrix flow represented by equation (4) is approximated by a step-wise calculation of particle paths;

$$\begin{pmatrix} x_{t+\Delta t} \\ y_{t+\Delta t} \end{pmatrix} = \begin{pmatrix} 1 + \Delta e & \Delta w \\ -\Delta w & 1 - \Delta e \end{pmatrix} \begin{pmatrix} x_t \\ y_t \end{pmatrix}, \qquad (9)$$

using small Δe and Δw. In this case, the kinematical vorticity number (5) can also be approximated by $\Delta w / \Delta e$.

Firstly, the outline of the rigid grain is defined by regularly spaced points (X_i, Y_i) (Fig. 2a). Next, consider the displaced positions of these points (x_i, y_i) for an incremental step, assuming that the grain has the same ductility as the matrix;

$$\begin{pmatrix} x_i \\ y_i \end{pmatrix} = \begin{pmatrix} 1 + \Delta e & \Delta w \\ -\Delta w & 1 - \Delta e \end{pmatrix} \begin{pmatrix} X_i \\ Y_i \end{pmatrix}. \qquad (10)$$

Since the rigid grain undergoes rotation and translation only, new positions for the rigid grain (X_i', Y_i') are represented by

$$\begin{pmatrix} X_i' \\ Y_i' \end{pmatrix} = \begin{pmatrix} \cos \Delta\theta & \sin \Delta\theta \\ -\sin \Delta\theta & \cos \Delta\theta \end{pmatrix} \begin{pmatrix} X_i \\ Y_i \end{pmatrix} + \begin{pmatrix} \Delta u \\ \Delta v \end{pmatrix} \qquad (11)$$

The rotation $(\Delta\theta)$ and translation $(\Delta u, \Delta v)$ are determined so as to minimize the expression

$$\sum_i \sqrt{(x_i - X_i')^2 + (y_i - Y_i')^2}. \qquad (12)$$

This implies that the gaps, overlaps and boundary sliding between grains and the matrix are minimized. The gaps which still remain are assumed to be filled by fibrous
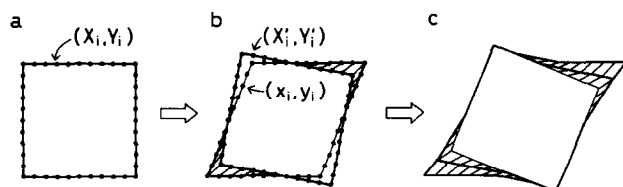

Fig. 2. Simulation model for the rigid crinoid-type pressure fringe. (a) The outline of the rigid grain before a deformation increment is defined by points (X_i, Y_i). (b) (x_i, y_i) are the positions of (X_i, Y_i) after a deformation increment, assuming no ductility contrast between grain and matrix. The position of the rigid grain (X_i', Y_i') after a deformation increment is determined so as to minimize the expression (12) and remaining gaps are filled by fibres. (c) The outline of the rigid grain is redefined and the next deformation step is computed.

minerals (Fig. 2b). Therefore, the crystallization rate and the rate of material supply are assumed to be high enough to keep pace with the strain rate. Furthermore, the growth direction is assumed to be parallel to the direction of relative displacement between the grain and the matrix.

Since a rigid crinoid-type pressure fringe is being simulated, the outline of the rigid grain is redefined to include the newly formed pressure fringe, then the next deformation step is computed (Fig. 2c).

The simulations are carried out for $\Delta e = 0.02$ and for variable degrees of non-coaxiality. In addition, the shape (R_0) and initial orientation (ϕ_0) of the rigid original grain and the total strain are also taken as variable parameters. The definitions of R_0 and ϕ_0 are as shown in Fig. 1. Up to 50 simulation steps (n) were taken.

The rotational behavior of a rigid elliptical grain in this simulation model is identical to that given by the theoretical equation (6).

GEOMETRY OF SIMULATED PRESSURE FRINGES

Circular grain $(R_0 = 1)$

Figure 3 shows the variation in the geometry of simulated pressure fringes for a circular original grain $(R_0 = 1)$. In the case of $W_k = 0$, a straight pressure fringe forms parallel to the x-axis, because the original grain does not rotate and the pressure fringe grows parallel to the x-axis throughout the deformation. In other cases $(W_k > 0)$, the pressure fringes develop curvature, because the original grains rotate, together with the previously formed pressure fringe, due to the vorticity of the flow and the growth direction of pressure fringe at each increment remaining sub-parallel to the x-axis.

In the present simulation, the curvature of the pressure fringes depends mainly on the rotation rate of the grains relative to the growth rate of the fringes, because of the absence of spin in the matrix flow. The sense of curvature is the same in all cases due to the same sense of vorticity, and thus of rotation of the grain. In this paper, this sense of curvature is called positive. Magnitude of curvature increases with increasing W_k.

Due to the growth of the pressure fringe, the shape of the composite grain (the original grain + pressure fringe) becomes gradually elongate in a direction sub-parallel to the principal axis of the strain ellipse. This elongation of the composite grain reduces the rotation rate of the grain due to an increasing ϕ_D component (equation 6) of anticlockwise sense. Therefore, the curvature of the pressure fringe decreases away from the original grain.

Elliptical grain $(R_0 = 2)$

(1) $W_k = 0$. Figure 4 shows the variation in the geometry of simulated pressure fringes for the case of $R_0 = 2$
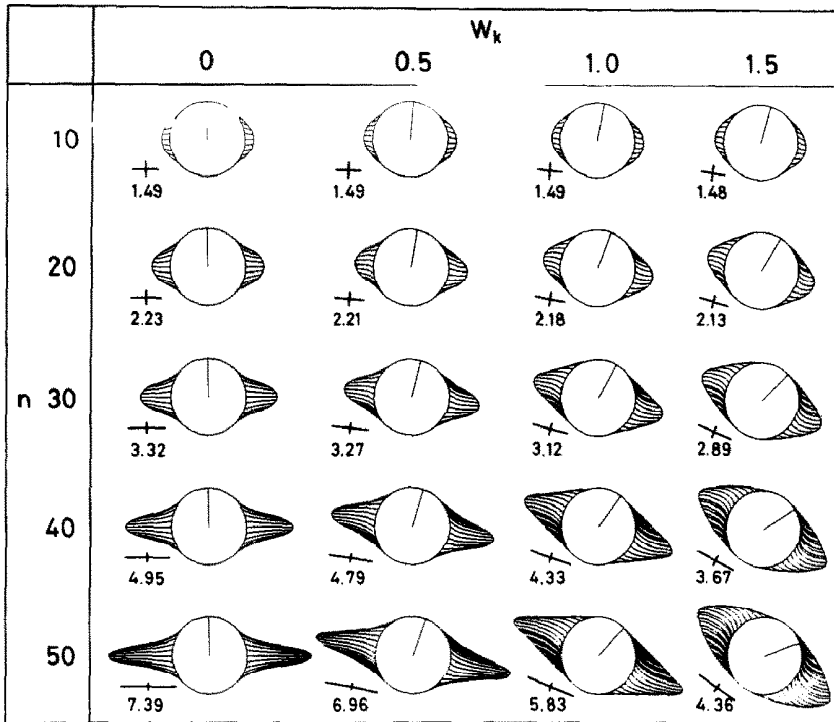
Fig. 3. Variation in the geometry of the simulated pressure fringes as a function of W_k and simulation step (n) for circular original grains ($R_0 = 1$). Radial marker lines indicate the rotation of the grains. The length and orientation of the principal axes of strain and the axial ratio of the total strain ellipse are shown to the lower left of each simulated pressure fringe.
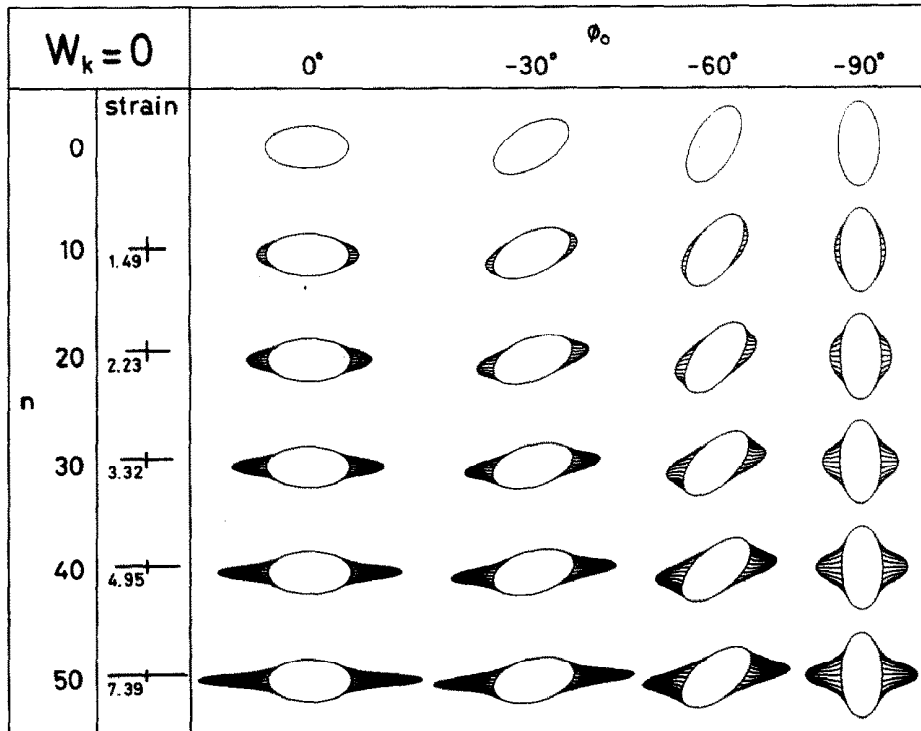

Fig. 4. Variation in the geometry of simulated pressure fringes as a function of initial orientation of the original grain (ϕ_0) and n for $W_k = 0$ and elliptical original grains ($R_0 = 2$). The principal axes and the axial ratio of the strain ellipse are shown in the left column.

and $W_k = 0$. Although the matrix flow is coaxial, the elliptical shape of the original grains gives rise to their rotation as a function of their initial orientation (ϕ_0). Since the variation in these rotation rates and the geometry of the developed pressure fringes as a function of ϕ_0 are symmetrical with respect to $\phi_0 = 0°$, only the cases for $-90° \leqslant \phi_0 \leqslant 0°$ are shown.

For this range of ϕ_0, the original grains rotate clockwise and pressure fringes grow with positive curvature, except for $\phi_0 = 0°$ and $-90°$, in which cases the grains do not rotate and straight pressure fringes are formed. The rotation of the composite grains and the growth of the pressure fringes cause a change in the shape and orientation of the composite grains, resulting in a change in
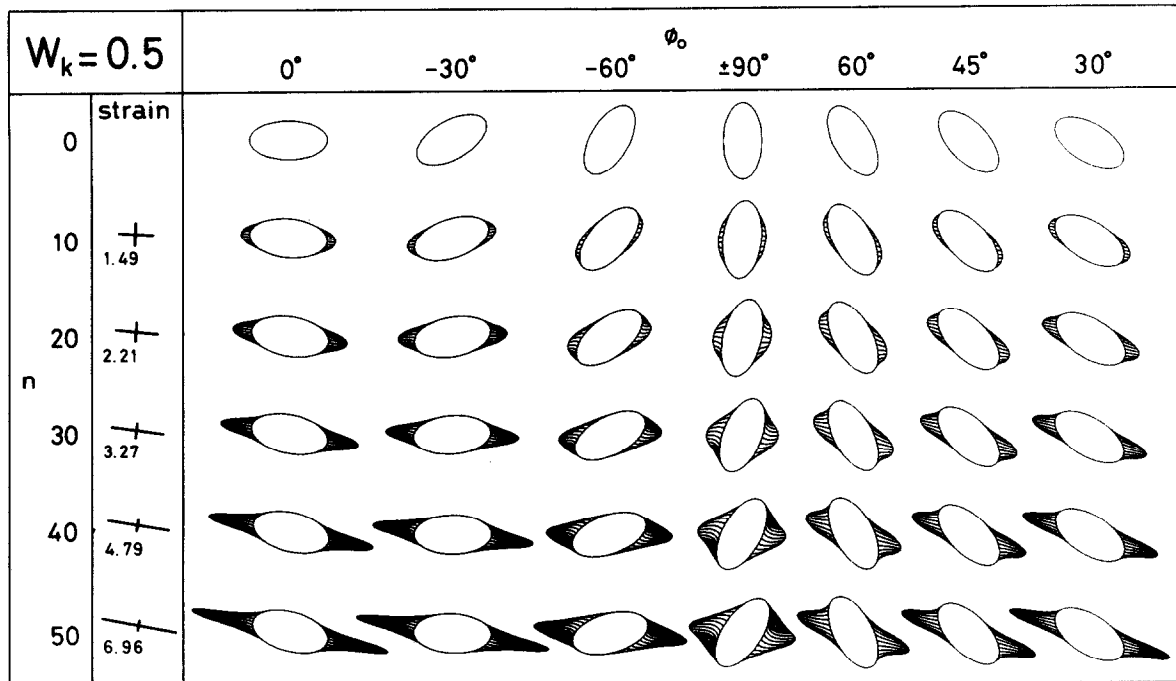
Fig. 5. Variation in the geometry of simulated pressure fringes as a function of ϕ_0 and n for $W_k = 0.5$ and $R_0 = 2$. The principal axes and the axial ratio of the strain ellipse are shown in the left column.
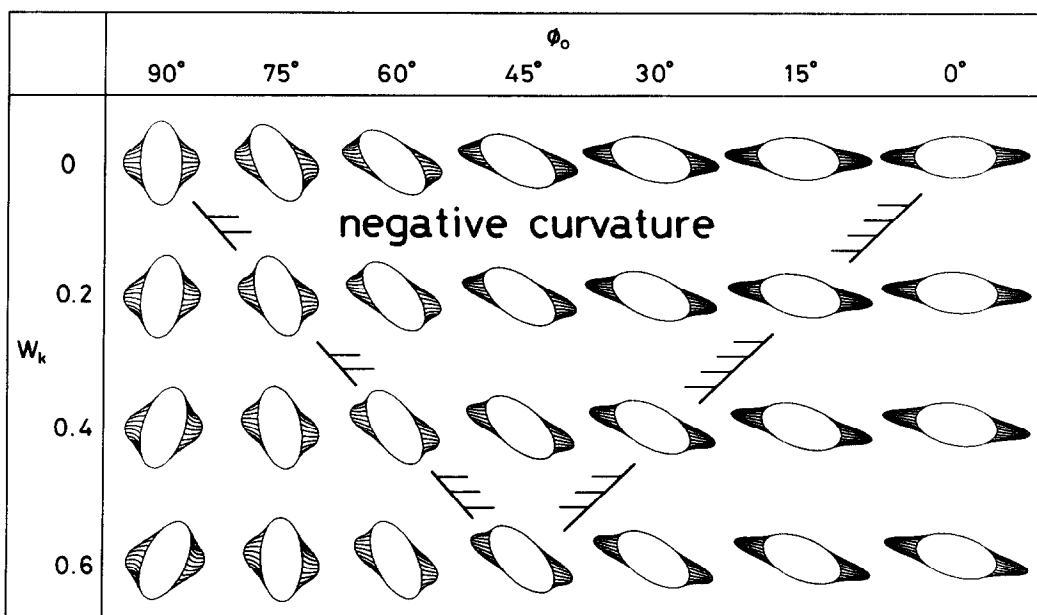
Fig. 6. Variation in the geometry of simulated pressure fringes for a range of ϕ_0 ($0° \leq \phi_0 \leq 90°$) and W_k ($0 \leq W_k \leq 0.6$) and for $R_0 = 2$ at $n = 30$. The range of values of ϕ_0 and W_k that give negative curvature of the pressure fringe is also shown.

the rotation rate during deformation. This change in rotation rate is responsible for the variation of curvature of the pressure fringes along the growth direction. For example, for the grain with $\phi_0 = -60°$, the curvature of the pressure fringe during the early stages ($n < 20$) is large, and it decreases in later stages due to the change in orientation of the composite grain.

(2) $0 < W_k < 1$. Figure 5 shows the variation in the geometry of simulated pressure fringes for the case of $R_0 = 2$ and $W_k = 0.5$. In spite of the non-coaxial deformation, the pressure fringes are nearly straight, except for $\phi_0 = \pm 90°$. Equation (8) indicates the anticlockwise rotation of the original grain with $\phi_0 = 45°$ at this R_0 and

W_k. However, this rotation rate is very small and the resulting pressure fringes are nearly straight.

Figure 6 shows the variation in the geometry of the pressure fringes at simulation step $n = 30$ in the range of $0° \leq \phi_0 \leq 90°$ and $0 \leq W_k \leq 0.6$ for $R_0 = 2$. The sense and magnitude of the curvature varies depending on the sense and magnitude of the rotation of the grains. The range of ϕ_0 for pressure fringe with negative curvature decreases with increasing W_k. However, the curvatures are small, reflecting small rotation rates. This variation in the geometry of the pressure fringes is a direct reflection of the rotational behavior of the grains, which can be represented by equations (6)–(8).
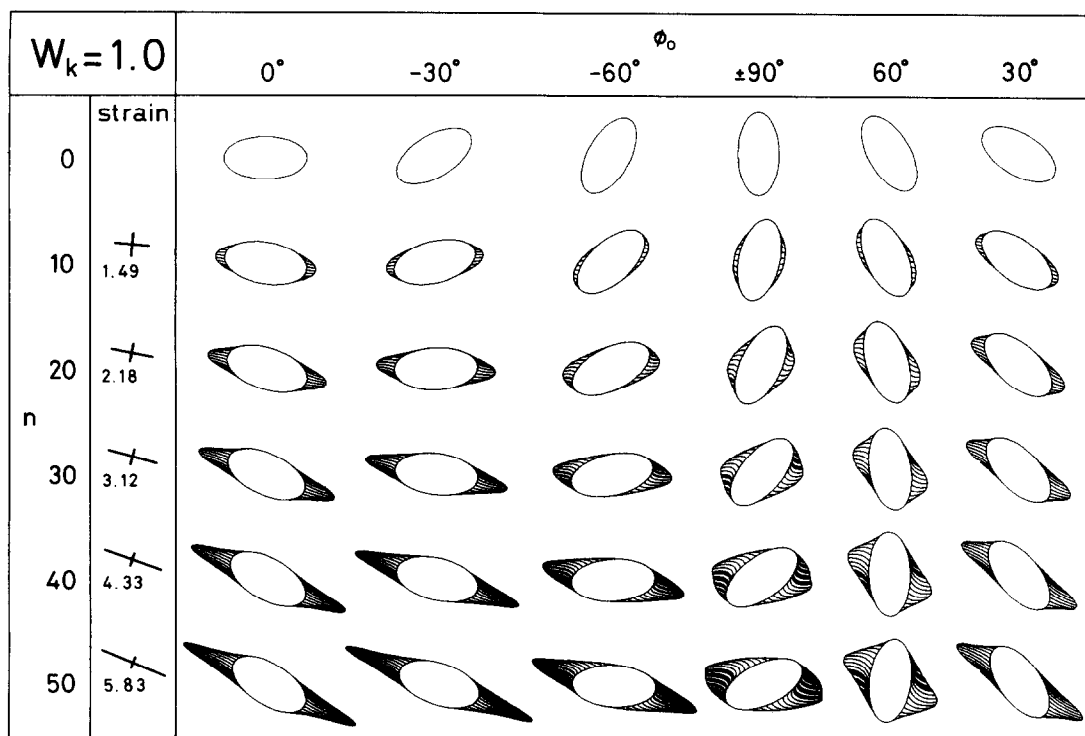
Fig. 7. Variation in the geometry of simulated pressure fringes as a function of ϕ_0 and n for W_k 1.0 and $R_0 = 2$. The principal axes and the axial ratio of the strain ellipse are shown in the left column.

(3) $W_k = 1$. Figure 7 shows the variation in the geometry of simulated pressure fringes for the case of $R_0 = 2$ and $W_k = 1$. In this case, the original grains rotate clockwise for all ϕ_0. The magnitude of the curvature of the pressure fringes varies with ϕ_0 and n. Generally, the curvature decreases away from the original grains due to the elongation of the composite grain subparallel to the finite strain axis during the deformation. For $\phi_0 = 60°$ and 90°, however, a nearly equiaxial shape of the composite grain allows for large rotation rates until later stages, resulting in large total curvature. In contrast, for ϕ_0 of around 0°, pressure fringes are nearly straight even from the beginning of growth, because the orientation of the composite grain is sub-parallel to the strain axis from an early stage.

(4) $W_k = 1.5$. For the case of $R_0 = 2$ and $W_k = 1.5$, variation in the geometry of simulated pressure fringes (Fig. 8) is similar to the case of $W_k = 1$. However, the effect of increasing non-coaxiality is represented by a general increase in the curvature of the pressure fringes. In particular, the circular shape of the composite grain and large curvature in the outer part of the fringe for $30° \leqslant \phi_0 \leqslant 90°$ are characteristic.

To summarize the present simulations, the following factors affect the geometry of the pressure fringe:

(1) The matrix flow pattern. Generally, the curvature of the pressure fringes increases with W_k.

(2) The total strain. A pressure fringe grows monotonously with straining, unless other destructive processes, such as dissolution of fringe material by intergranular fluid, are involved.

(3) The shape and orientation of the original grain. The curvature of the pressure fringe depends on the

rotation rate of the grain, which is a function of these parameters.

(4) The shape and orientation of the composite grain. The growth of a pressure fringe causes a change in the shape and orientation of the composite grain, affecting the next growth increment.

METHOD FOR THE DETERMINATION OF FLOW PARAMETERS

So far, the variation in the geometry of simulated pressure fringes as a function of several parameters, such as W_k, R_0, ϕ_0 and total strain, have been described. Next, I discuss how these parameters can be determined from the final geometry of pressure fringes.

Qualitatively, the sense and magnitude of the pressure fringe curvature reflect the sense and value of W_k, and the shape of the composite grain reflects the strain ellipse. However, since several parameters contribute to the geometry of a pressure fringe, there is no one-to-one correspondence between these. We must remember that the available information is restricted to the final shape and orientation of the original grains and the pressure fringes.

Figure 9 shows variation in the geometry of pressure fringes after 30 simulation steps, as a function of W_k and the final orientation of the original grain relative to the principal strain axis ($\phi'_{n=30} = 0°$, $-45°$, 90° and 45°). In this figure, the long axis of the strain ellipse is horizontal.

For $\phi'_{n=30} = 0°$, nearly straight pressure fringes are developed parallel to the strain axis. Since the curvature of the pressure fringe is very small even for $W_k = 1.5$, it
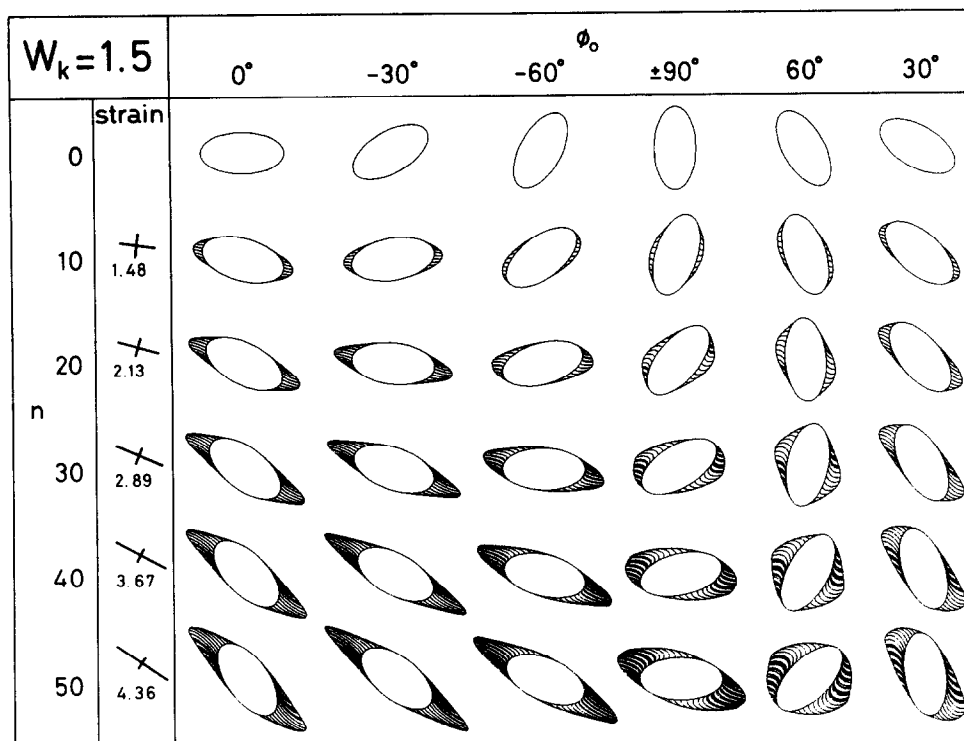
Fig. 8. Variation in the geometry of simulated pressure fringes as a function of ϕ_0 and n for $W_k = 1.5$ and $R_0 = 2$. The principal axes and the axial ratio of the strain ellipse are shown in the left column.
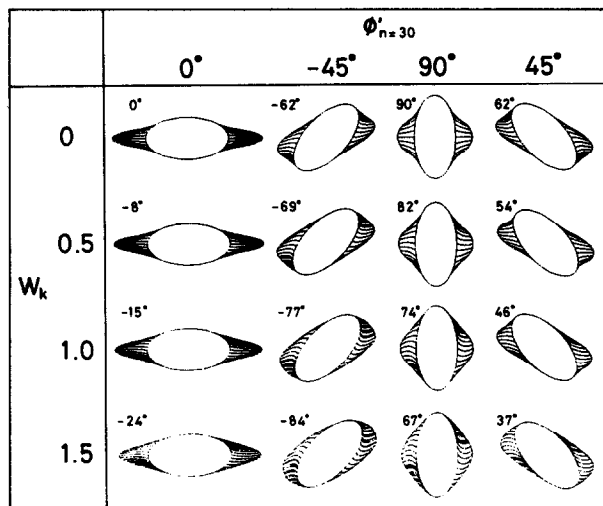

Fig. 9. Variation in the geometry of simulated pressure fringes at $n = 30$ as a function of W_k and final orientation of the elliptical ($R_0 = 2$) original grain with respect to the principal strain axis ($\phi'_{n=30}$). The long axis of the strain ellipse is horizontal. The initial orientation of the original grain (ϕ_0) is shown in the upper left of each simulated pressure fringe.

is difficult to determine the value of W_k from these grains. However, a nearly straight pressure fringe parallel to the long axis of the original grain indicates the principal axis of strain ellipse irrespective of the values of W_k, ϕ_0 and the total strain.

For large $\phi'_{n=30}$, by contrast, there is a large variation in the curvature of the pressure fringes depending on the value of W_k. Therefore, a pressure fringe with such an orientation of the original grain is suitable for the determination of W_k. In addition, comparison between pressure fringes around grains whose original shapes are

symmetrically orientated with respect to the strain axis leads to a clearer distinction of W_k. For example, the geometry of the pressure fringes with $\phi'_{n=30} = -45°$ and 45° and $W_k = 0$ are mirror images of each other. The difference in the geometry of pressure fringes with these orientations of the original grains increases with W_k. Furthermore, the presence of different senses of curvature of pressure fringes indicates a value of W_k smaller than 1 (Fig. 6). A larger number of pressure fringes of variable shape and orientation of the original grain limit the value of W_k to a narrower range. However, in practice this criterion may not be effective for W_k values larger than 0.5.

Consequently, a general method for the determination of flow parameters is as follows. First, the orientation of the principal strain axis is determined by the grain with nearly straight pressure fringes parallel to the long axis of the original grain. Then, the sense and value of W_k are determined using several pressure fringes around original grains with long axes at a high angle to the principal strain axis. The total strain is estimated from the length of the pressure fringes, taking the shape and orientation of the original grains into account. Thus, one pressure fringe is not sufficient to determine the flow parameters. The method requires the assumption of homogeneous bulk deformation in the domain including all grains used in the analysis.

NATURAL EXAMPLES

The examples come from an outcrop of Upper Paleozoic limestone at Nagasaka, in the South Kitakami Mountains, northeast Japan. Strata in this area are

mainly composed of shallow marine sedimentary and volcanic rocks (Onuki 1981), and they were folded, cleaved and intruded by granitic bodies during the Early Cretaceous (Oho 1981, 1982, Ikeda 1984, Ishii 1985, 1988a, b, 1990, Kanagawa 1986, 1991).

The studied samples contain variable amounts of tuffaceous material and range from massive pure limestone to highly impure foliated limestone rich in chlorite. A slaty cleavage defined by the preferred orientation of chlorite trends N–S and dips steeply west. A stretching lineation on the cleavage is nearly horizontal.

The limestones include dusty (rich in impurities) calcite grains, most of which are crinoid segments or fragments, in a matrix of fine grained calcite and chlorite. Pressure fringes are developed on these grains, particularly in rocks with a moderate content of tuffaceous material. As a general tendency, purer limestones show evidence of intra-crystalline deformation mechanisms, such as kinking and twinning, and of fracturing of calcite grains. In contrast, in highly impure limestones, the foliation wraps around the scattered calcite grains without the development of pressure fringes. In addition, limestones with moderate to high chlorite content show evidence of pressure solution such as truncation of calcite grains by slaty cleavage. These features may indicate that the development of pressure fringes requires a suitable rheological contrast between the grain and the matrix.

Photomicrographs of pressure fringes in two samples, and line drawings from them, are shown in Figs. 10 and 11. The fringes are mainly composed of calcite, which is optically continuous with the original grains, indicating that these pressure fringes are of crinoid type. The fringes can be distinguished from the original grain by their inclusion-free clean appearance.

Those original grains and pressure fringes that show evidence of intra-crystalline deformation, such as wavy extinction, kinking, fracturing and pressure solution, are excluded from the analysis. Many calcite fringes are intergrown with thin chlorites, providing a marker of growth direction, which is considered to be the relative displacement direction between the grain and the matrix. The fringes of pure calcite cannot be used in the analysis because of the absence of a marker of the growth direction. Some pressure fringes are of composite type, with calcite growing from the original grain and chlorite growing from the matrix (e.g. Figs. 10e & h). The chlorite aggregates in these fringes are elongate parallel to the slaty cleavage, indicating that they are deformable. Since part of the gap has been filled by calcite and the rest by chlorite in these composite fringes, the size of the rigid composite grain (original grain + calcite fringes) is smaller than in the simulation model. Therefore, composite type pressure fringes with large proportions of chlorite are also excluded from the analysis.

All pressure fringes composed of calcite show the same curvature sense (negative), irrespective of shape and orientation of the original grains, but the magnitude of curvature does vary with these parameters.

The orientation of the original grains with nearly straight pressure fringes parallel to their long axes are parallel to slaty cleavage (Figs. 10a & f). This indicates that the long axis of the finite strain ellipse for the matrix flow during the growth of the pressure fringes is parallel to slaty cleavage. Pressure fringes on original grains at a high angle to the slaty cleavage (Figs. 10b, d & g) and on nearly circular original grains (Figs. 10c, e & h), show moderate to large curvatures. These variations in pressure-fringe curvature as a function of shape and orientation of the original grain almost match the results of the simulation for $W_k = -1$. Note in particular the large curvature of the pressure fringes in Figs. 10(d) & (g) compared with the small curvature in Fig. 10(b) (see also Fig. 9) and the decreasing curvature away from the original grains in Figs. 10(c), (e) & (h).

The conclusion is that these pressure fringes are estimated to have formed under approximately progressive sinistral simple shearing conditions. In addition, the axial ratio of the strain ellipse can be estimated to be 4–5 from the length of the pressure fringes.

In sections normal to the lineation and in sections parallel to the slaty cleavage, little pressure fringe growth is observed, indicating a slight deviation from plane strain conditions.

DISCUSSION

In this paper, the following assumptions have been made in determining the flow parameters:

(1) The deformation is two dimensional (i.e. plane strain) and constant area is maintained.

(2) The growth direction of the pressure fringe is parallel to the direction of relative displacement between the grain and the matrix.

(3) The matrix flow is homogeneous, even immediately around the rigid grain.

(4) The grain and the pressure fringe behave in a rigid manner.

(5) The crystallization rate is commensurate with the strain rate.

(6) The matrix flow pattern is constant with no spin component during the deformation.

(7) The matrix flow is homogeneous within a volume including the analyzed pressure fringes.

Assumptions (1)–(5) are intrinsic to the present simulation model. On the other hand, Assumptions (6) and (7) are not necessary for the model. The model can be applied to any time-dependent deformation path, by changing the flow parameters for each increment. However, this leads to a ridiculous increase in the number of parameters to be determined, and these parameters must be determined by trial and error. The present method can avoid this by making use of Assumptions (6) and (7) and by using the systematic variation in the geometry of the pressure fringes as a function of the shape and orientation of the original grains as a criterion of match to the model.

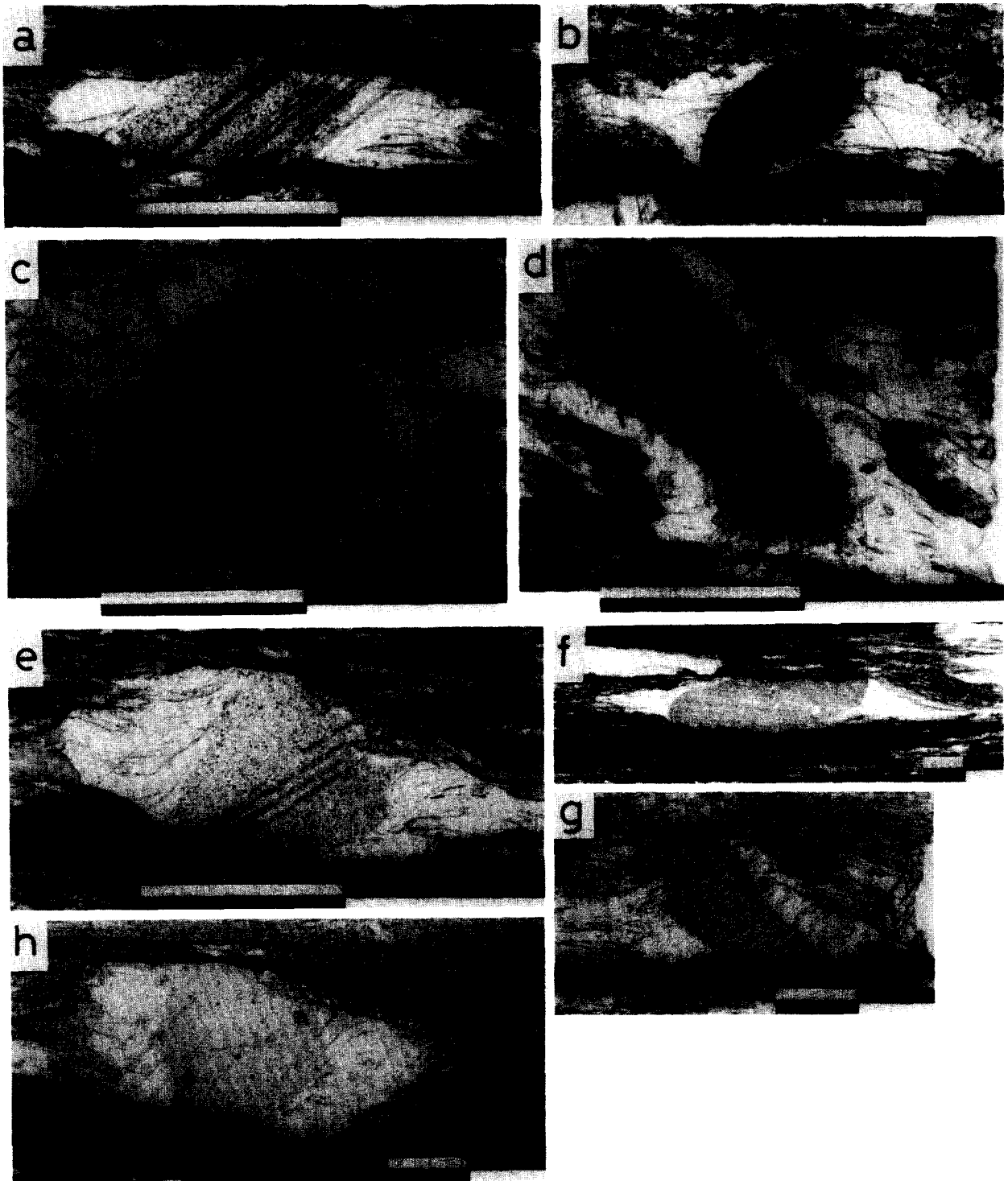As described above, Assumptions (2) and (4) hold for

Fig. 10. Photomicrographs of pressure fringes around calcite grains set in a matrix of fine-grained calcite and chlorite. The fringes consist of calcite in optical continuity with the original calcite grains, and chlorite. The plane of observation is normal to slaty cleavage and parallel to lineation and the view is downward. Traces of slaty cleavage are horizontal. The samples come from Upper Paleozoic limestones in the South Kitakami Mountains, northeast Japan. (a)–(e) from one sample and (f)–(g) from a second sample. All scale bars are 1 mm.
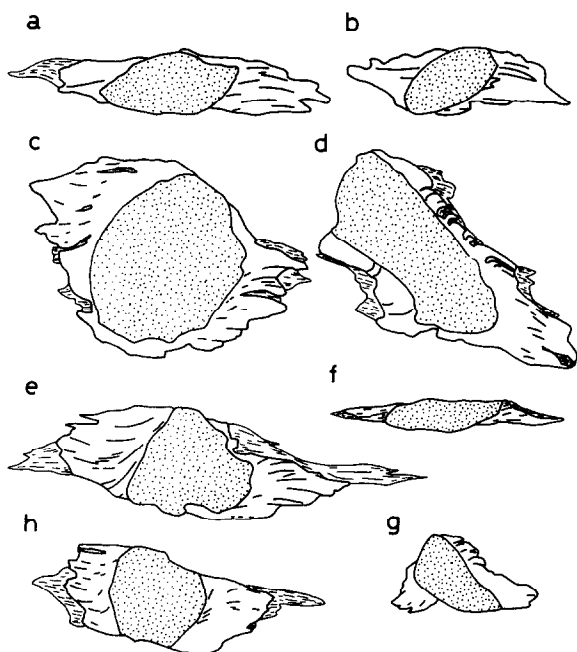
Fig. 11. Line drawings from the photomicrographs shown in Fig. 10. Chlorite in the fringes is indicated by thin lines.
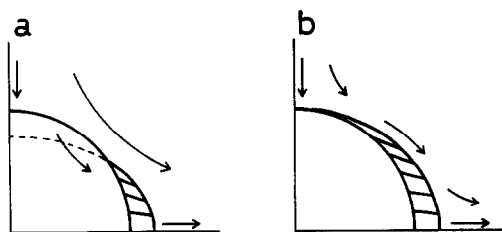

Fig. 12. Flow in the matrix around the rigid grain and growth of pressure fringes for the present simulation model (a) and for an actual case (b). A homogeneous matrix flow in the model causes a narrow pressure fringe compared with the actual one.

the present natural examples. Furthermore, Assumptions (5), (6) and (7) are considered to nearly hold from the consistency of the variation in the geometry of the natural pressure fringes with the simulations.

Assumption (1) may be a most critical condition for the general application of the method to natural examples. The three-dimensional shape of the original grain can cause rotation of the grain around an axis oblique to the plane of observation, even if the matrix deformation is plane strain (Jeffery 1922, Freeman 1985, Busa & Gray 1992). In this case, the growth direction of the pressure fringes will be oblique to the plane. In addition, growth of pressure fringes involves mass transfer of fibre material a certain distance, probably through inter-granular fluids. This may lead to net volume change.

Contrary to Assumption (3), the matrix flow is disturbed around the rigid grain. The pressure fringes in the model show a rather abrupt tapering compared with the natural examples. This difference may be a result of this assumption, as shown in Fig. 12.

The flow around a rigid grain may be complex and has not been realized except for simple cases. For example,

Masuda & Ando (1988) calculated the matrix flow around a rigid spherical grain under a coherent boundary condition between grain and matrix. However, in the development of pressure fringes, the matrix separates from the grain. This separation may affect both the matrix flow around the grain and the rotational behavior of the grain. The effect of this on the geometry of the pressure fringes is not clear.

In conclusion, crinoid-type pressure fringes are useful for the determination of non-coaxiality, although further studies are needed: (1) for the application to general flows, such as three-dimensional flows with volume change and time-dependent flow parameters, and (2) of the physical processes involved.

REFERENCES

Beutner, E. C. & Diegel, F. A. 1985. Determination of fold kinematics from syntectonic fibers in pressure shadows, Martinsburg slate, New Jersey. *Am. J. Sci.* **285**, 16–50.

Bjornerud, M. 1989. Toward a unified conceptual framework for shear-sense indicators. *J. Struct. Geol.* **11**, 1045–1049.

Busa, M. D. & Gray, N. H. 1992. Rotated staurolite porphyroblasts in the Littleton Schist at Bolton, Connecticut, U.S.A. *J. Metamorph. Geol.* **10**, 627–636.

Cobbold, P. R., Gapais, D., Means, W. D. & Treagus, S. H. (Editors) 1987. Shear criteria in rocks. *J. Struct. Geol.* **9**, 521–778.

Cox, S. F. 1987. Antitaxial crack-seal vein microstructures and their relationship to displacement paths. *J. Struct. Geol.* **9**, 779–787.

Cox, S. F. & Etheridge, M. A. 1983. Crack-seal fibre growth mechanisms and their significance in the development of oriented layer silicate microstructures. *Tectonophysics* **92**, 147–170.

Dennis, A. J. & Secor, D. T. 1987. A model for the development of crenulations in shear zones with applications from the Southern Appalachian Piedmont. *J. Struct. Geol.* **9**, 809–817.

Durney, D. & Ramsay, J. G. 1973. Incremental strains measured by syntectonic crystal growths. In: *Gravity and Tectonics* (edited by De Jong, K. A. & Scholten, R.). Wiley, New York, 67–96.

Elliott, D. 1972. Deformation paths in structural geology. *Bull. geol. Soc. Am.* **83**, 2621–2638.

Ellis, M. A. 1986. The determination of progressive deformation histories from antitaxial syntectonic crystal fibres. *J. Struct. Geol.* **8**, 701–709.

Etchecopar, A. & Malavieille, J. 1987. Computer models of pressure shadows: a method for strain measurement and shear-sense determination. *J. Struct. Geol.* **9**, 667–677.

Freeman, B. 1985. The motion of rigid ellipsoidal particles in slow flows. *Tectonophysics* **113**, 163–183.

Ghosh, S. K. & Ramberg, H. 1976. Reorientation of inclusions by combination of pure shear and simple shear. *Tectonophysics* **34**, 1–70.

Goldstein, A. G. 1988. Factors affecting the kinematic interpretation of asymmetric boundinage in shear zones. *J. Struct. Geol.* **10**, 707–715.

Hanmer, S. 1986. Asymmetrical pull-aparts and foliation fish as kinematic indicators. *J. Struct. Geol.* **8**, 111–122.

Ikeda, Y. 1984. Study on the Early Cretaceous tectonic movement in the Southern Kitakami Massif, Northeast Japan. *Geol. Rep. Hiroshima Univ.* **24**, 99–157. (In Japanese with English abstract.)

Ishii, K. 1985. Development of fold and slaty cleavage in the Oshika Peninsula, the South Kitakami Mountains. *J. geol. Soc. Japan* **91**, 309–321. (In Japanese with English abstract.)

Ishii, K. 1988a. Grain growth and re-orientation of phyllosilicate minerals during the development of slaty cleavage in the South Kitakami Mountains, northeast Japan. *J. Struct. Geol.* **10**, 145–154.

Ishii, K. 1988b. Development of slaty cleavage and emplacement of granitic bodies in the South Kitakami Mountains, Japan. *Tohoku*

Univ., Inst., Geol. Paleont., Contr. **91**, 1–14. (In Japanese with English abstract.)

Ishii, K. 1990. Left-lateral shearing estimated from pressure fringe, in the South Kitakami Mountains, northeast Japan. *J. Geol. Soc. Japan* **96**, 475–478. (In Japanese.)

Ishii, K. 1992. Partitioning of non-coaxiality in deforming layered rock masses. *Tectonophysics* **210**, 33–43.

Jeffery, G. B. 1922. The motion of ellipsoidal particles immersed in a viscous fluid. *Proc. R. Soc. Lond.* **A102**, 161–179.

Kanagawa, K. 1986. Early Cretaceous folding and cleavage in the Kitakami Mountains, analyzed in the Ofunato terrane. *J. Geol. Soc. Japan* **92**, 349–370.

Kanagawa, K. 1991. Change in dominant mechanisms for phyllosilicate preferred orientation during cleavage development in the Kitakami slates of NE Japan. *J. Struct. Geol.* **13**, 927–943.

Lister, G. S. & Snoke, A. W. 1984. S–C mylonites. *J. Struct. Geol.* **6**, 617–638.

Lister, G. S. & Williams, P. F. 1983. The partitioning of deformation in flowing rock masses. *Tectonophysics* **92**, 1–33.

Malavieille, J. & Ritz, J. F. 1989. Mylonitic deformation of evaporites in décollements: examples from the Southern Alps, France. *J. Struct. Geol.* **11**, 583–590.

Masuda, T. & Ando, S. 1988. Viscous flow around a rigid spherical body: a hydrodynamical approach. *Tectonophysics* **148**, 337–346.

Means, W. D., Hobbs, B. E., Lister, G. S. & Williams, P. F. 1980. Vorticity and non-coaxiality in progressive deformations. *J. Struct. Geol.* **2**, 371–378.

Oho, Y. 1981. Slaty cleavage textures in the Ojika Peninsula, the South Kitakami Mountains. *J. Geol. Soc. Japan* **87**, 657–673. (In Japanese with English abstract.)

Oho, Y. 1982. Effective factors controlling cleavage formation and other microstructures in the South Kitakami Mountains. *J. Fac. Sci. Univ. Tokyo* **20**, 345–381.

Onuki, Y. 1981. The Kitakami Mountains. In: *Explanatory Text of the Geologic Map around the Kitakami River in the Scale* 1:200,000. Hase Geological Survey Inc., Sendai, 3–223. (In Japanese.)

Passchier, C. W. 1986. Flow in natural shear zones—the consequences of spinning flow regimes. *Earth & Planet. Sci. Lett.* **77**, 70–80.

Passchier, C. W. 1988. Analysis of deformation paths in shear zones. *Geol. Rdsch.* **77**, 309–318.

Passchier, C. W. 1990. Reconstruction of deformation and flow parameters from deformed vein sets. *Tectonophysics* **180**, 185–199.

Passchier, C. W. & Simpson, C. 1986. Porphyroclast systems as kinematic indicators. *J. Struct. Geol.* **8**, 831–843.

Passchier, C. W. & Sokoutis, D. 1993. Experimental modelling of mantled porphyroclasts. *J. Struct. Geol.* **15**, 895–909.

Ramsay, J. G. 1980. The crack-seal mechanism of rock deformation. *Nature* **284**, 135–139.

Ramsay, J. G. & Huber, M. 1983. *The Techniques of Modern Structural Geology, Vol. 1: Strain Analysis.* Academic Press, London.

Simpson, C. & De Paor, D. G. 1993. Strain and kinematic analysis in general shear zones. *J. Struct. Geol.* **15**, 1–20.

Simpson, C. & Schmid, S. M. 1983. An evaluation of criteria to deduce the sense of movement in sheared rocks. *Bull. geol. Soc. Am.* **94**, 1281–1288.

Spencer, S. 1991. The use of syntectonic fibres to determine strain estimates and deformation paths: an appraisal. *Tectonophysics* **194**, 13–34.

Truesdell, C. 1953. Two measures of vorticity. *J. Rational Mech. Anal.* **2**, 173–217.

Wickham, J. S. 1973. An estimate of strain increments in a naturally deformed carbonate rock. *Am. J. Sci.* **273**, 23–47.

Williams, P. F. & Price, G. P. 1990. Origin of kinkbands and shear-band cleavage in shear zones: an experimental study. *J. Struct. Geol.* **12**, 145–164.